Hydrodynamic investigation of a fixed OWC Wave Energy Converter

De-Zhi Ning, Rong-Quan Wang, Bin Teng
State Key Laboratory of Coastal and Offshore Engineering, Dalian University of Technology, Dalian, 116024, China

Jun Zang, Li-Fen Chen
WEIR Research Unit, Department of Architecture and Civil Engineering, University of Bath, Bath BA2 7AY, UK.
Email: dzning@dlut.edu.cn

Highlights:

- Hydrodynamics of a stationary OWC device was investigated experimentally.
- The air-fluid interaction in an OWC chamber was modeled with an improved nonlinear potential model.
- Some interesting results have been observed for free surface elevations, pressure distributions and hydrodynamic efficiencies for a range of conditions.

1. Introduction

The oscillating water column (OWC) device is one of the most successful wave energy converters due to its mechanical and structural simplicity (Veigas, et al., 2014), and has been extensively studied and implemented (Iturrioz, et al., 2014). Generally, the fundamental component of an OWC device is a partially submerged chamber, which is used to trap a column of air above the free surface. As the waves impinge on the device, the oscillating motion of the internal water forces the air trapped inside the chamber to flow through a turbine that drives an electrical generator. In the case of a land-based OWC, the incident wave energy is altered by the combined effects of wave refraction, wave shoaling, wave breaking and bottom friction when waves propagate towards the shoreline. Therefore, it is of practical importance to investigate and fully understand the hydrodynamic performance of the OWC devices.

In this study, the hydrodynamics of a stationary OWC wave energy device subject to various sea states and geometric parameters is investigated both experimentally and numerically. The free surface elevations inside and outside the chamber, air pressure in the chamber and wave pressures on the front wall were investigated. The viscous effects on the hydrodynamic efficiency and resonant frequency were also studied.

2. Experimental and numerical models

2.1 Experimental Set-ups

The physical model tests were carried out in the wave-current flume at Dalian University of Technology, China. The glass-walled wave flume is 69 m long, 2 m wide and 1.8 m deep. The flume is divided into two sections along the longitudinal direction, which are measured as 1.2 m and 0.8 m in width, respectively. The OWC model was installed in the 0.8 m wide section and 50 m away from the wave maker.

The schematic of the experimental setup is shown in Fig.1. The following paramenters were defined in the experiments, water depth h = 0.8m, the chamber width B = (0.55 m, 0.70 m and 0.85m), the thickness of the front wall C = 0.04 m, the diameter of the orific D = (0.04 m, 0.06 m and 0.08m), the draft of the front wall d = (0.14 m, 0.17m and 0.20 m), the height of the chamber above the still water h_c = 0.20 m. An array of resistance-type wave gauges were used to record the instantaneous surface elevations at four locations, and six pressure sensors were installed on the front wall of the chamber to measure the wave pressures. The air pressure inside the chamber was measured by two pressure sensors installed on the each side of the orifice. The layout of the wave guages and the pressure senor can also be found in Fig.

1. Both the free surface elevation and pressure signals are sampled at 50 Hz. Six wave amplitudes A_i in the scope of (0.02 m, 0.07 m) and fourteen wave periods T in the scope of (0.95 s, 2.35 s) are considered in the experiment.

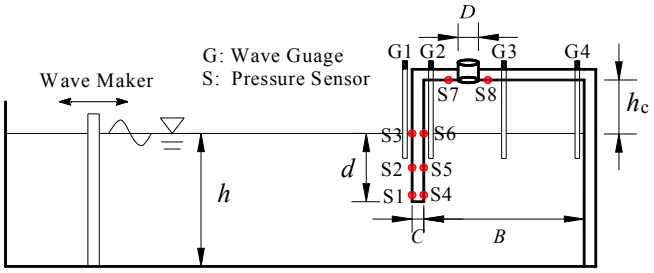

Fig. 1 Schematic of the experimental setup.

2.2 Numerical model

With the assumption that the fluid is ideal, a 2-D fully nonlinear numerical model, which is based on potential theory and the higher-order boundary element method (HOBEM), is developed to reproduce the experiments. The incident wave is generated via the inner-domain sources whose strength is related with the incident wave velocity. A damping layer with a coefficient $\mu_1(x)$ is applied at the left end of the numerical flume to minimize the wave reflection from the device. The governing equation is Poisson equation satisfied by the velocity potential. To take into account the viscous effect due to the water viscosity and the flow separation, an artificial viscous damping term represented by a coefficient μ_2 is introduced to the dynamic free surface boundary condition inside the OWC chamber. Therefore, velocity potential satisfies the following modified fully nonlinear free surface boundary conditions

$$\begin{cases} \dfrac{dX(x,z)}{dt} = \nabla\phi - \mu_1(x)\left(X - X_0\right) \\ \dfrac{d\phi}{dt} = -g\eta + \dfrac{1}{2}\left|\nabla\phi\right|^2 - \dfrac{p_a}{\rho} - \mu_1(x)\phi - \mu_2\dfrac{\partial\phi}{\partial n} \end{cases}, \tag{1}$$

where $X_0=(x_0, 0)$ denotes the initial static position of the fluid particle. The details about the determination of the damping coefficient $\mu_1(x)$ can be found in Ning et al. (2008). The artificial viscous damping coefficient μ_2 is determined by trial and error, and it is only applied inside the chamber.

The air pressure p_a on the water free surface is set to be zero (*i.e.*, atmospheric pressure) outside the chamber. The air pressure p_a inside the OWC chamber is calculated by applying the continuity equation to air flow inside the chamber during the volume change and assuming a linear relationship between the chamber pressure and the air duct velocity. Thus, the pneumatic pressure is given by

$$p_a(t) = C_{dm}U_d(t), \tag{2}$$

where C_{dm} is the linear pneumatic damping coefficient and $U_d(t)$ is the air flow velocity in the orifice.

The energy absorbed by the OWC device in the numerical model can be calculated by

$$P_0 = \frac{1}{T}\int_t^{t+T} Q(t)p(t)\,dt = \frac{1}{T}\int_t^{t+T} B\bar{\dot{\eta}}(t)p(t)\,dt = \frac{1}{T}\int_t^{t+T} C_{dm}U_d(t)AU_d(t)\,dt, \tag{3}$$

where the flow rate $Q(t)=B\bar{\dot{\eta}}(t)=AU_d(t)$, $\bar{\dot{\eta}}(t)$ is the time mean vertical velocity of the free surface inside the chamber. Then the hydrodynamic efficiency ξ can be obtained through P_0 divided by the incident wave energy.

The aforementioned boundary value problem can be converted into a boundary integral equation (BIE) as usual, i.e. via the second Green's theorem. The BIE is solved by the higher-order boundary element method using a set of collocation nodes (*i.e.*, three-node line elements) to discretize the entire curved boundary surface. Both the boundary geometry and

the physical variables are interpolated based on the nodal values and the quadratic shape functions within the boundary elements. Then the wave loads on the device can be obtained by integrating the pressure over the wetted surface of the object (Γ_b)

$$f_{x(z)} = -\rho \int_{\Gamma_b} \left(\frac{\partial \phi}{\partial t} + g\eta + \frac{1}{2} |\nabla \phi|^2 \right) n_{x(z)} d\Gamma , \tag{4}$$

in which the temporal derivative of the velocity potential is solved by the acceleration-potential method (Koo and Kim, 2007).

3. Results and discussions

In the numerical simulations, the length of the numerical flume is set to 5λ (where λ is the wave length), in which 1.0λ at the left side is used as the damping layer. By performing the convergence tests, the spatial step and temporal step are set as $\Delta x=\lambda/30$ and $\Delta t=T/80$ respectively. The viscous coefficient and the linear pneumatic damping coefficient are chosen as μ_2=0.4 and C_{dm}=9.5, respectively. The geometrical parameters of B = 0.7 m, D = 0.06 m and d = 0.14 m are kept unchanged for the results presented in this paper. For each case, 30 periods of waves are simulated.

The time series of the calculated and measured surface elevation at locations G1 and G3 are shown in Fig. 2 (a), and the wave pressures on the outer surface of the front wall for the case with T = 1.61 s and A_i = 0.03 m are shown in Fig.2(b). It can be observed from Fig.2 that good agreements between the numerical results and experimental measurements are achieved, which indicates that the present simplified pneumatic model can well model the interaction of water and air inside the chamber.

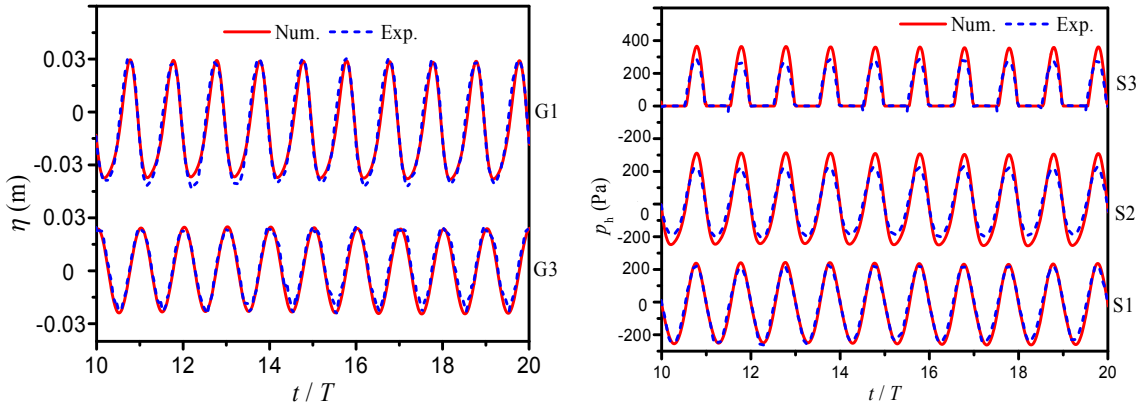

(a) Surface elevations at G1 and G3 (b) Pressures on the outer surface of the front wall

Fig.2 Time series of the predicted and observed free surface elevation in the chamber center and hydrodynamic pressure on the outer surface of the front wall.

Fig.3 shows the predicted pressure distributions on the front wall under the action of wave crest and wave trough for the wave with T = 1.61 s and A_0 = 0.03 m, respectively. It can be seen that the positive maximum pressure occurs at the position of transient surface on the outer surface of the front wall under the action of the wave crest, while the negative maximum pressure is at the bottom toe on the inner surface of the front wall under the action of the wave trough.

Fig. 4 shows the variation of the experimental maximum surface elevation with the dimensionless wavelength λ/B for all four spatial locations. It can be noted that the maximum surface elevations at three locations inside the chamber increase with the wavelength, while the maximum surface elevation at the location outside the chamber presents an opposite trend. The maximum surface elevation at the locations G2 and G4 reaches its maximum value at λ/B=2 (*i.e.* λ=1.40), while the relative maximum surface elevation at the chamber center, *i.e.* G3, is almost zero. This is due to the so-called seiching phenomenon excited at λ/B=2.

Fig.5 presents the variation of the hydrodynamic efficiency ξ with and without introduction of the damping term. It can be seen that the potential flow theory without the consideration of the viscous effect (μ_2= 0.0) over-predicts the

hydrodynamic efficiency, although the resonant frequency was well captured. In general, the potential flow model results calculated with an appropriate artificial damping agree well with the experimental data. The results have indicated that the hydrodynamic efficiency can reach over 60% in the region kh = 0.9-2.2.

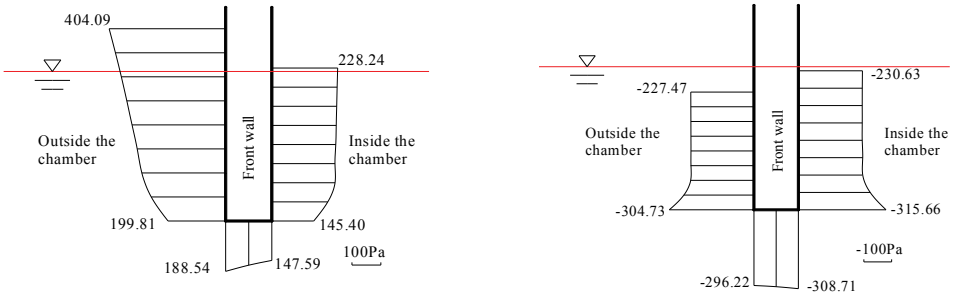

(a) Under the wave crest (b) Under the wave trough

Fig.3 Predicted pressure distributions on the front wall due to the wave crest and wave trough actions

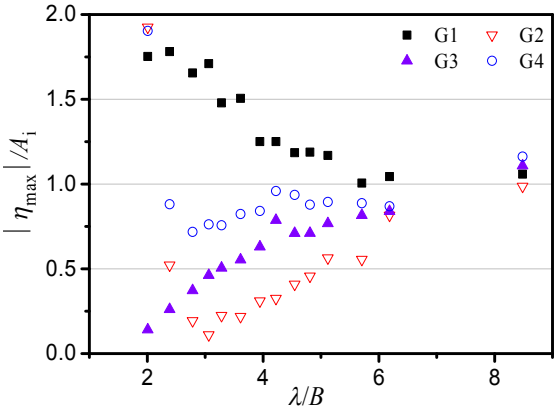

Fig. 4 Variation of the maximum surface amplitudes versus λ/B

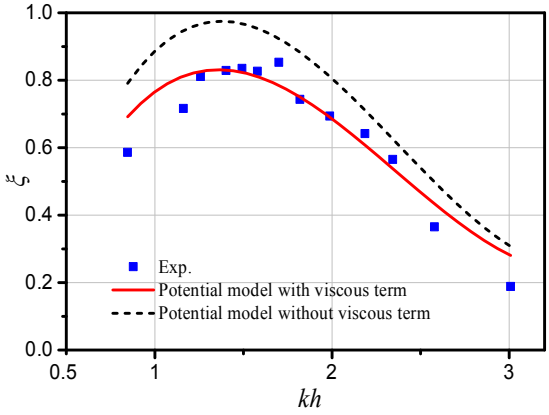

Fig.5 Variation of hydrodynamic efficiency with kh

4. Conclusions

The hydrodynamics of an OWC device is investigated both experimentally and numerically in this study. It is found that the water motion inside the chamber would induce the seiching phenomenon at λ/B=2. The comparisons between the experimental measurements and the solutions of the potential flow model with and without the artificial viscous term demonstrate that the fluid viscosity plays an important role in predicting the hydrodynamic efficiency of a fixed OWC. More examples and further investigation on the wave-interaction with an OWC will be presented at the workshop.

Acknowledgements

The authors would like to acknowledge financial support from the NSFC (Grant No. 51490672) and the Joint Project between NSFC and RS (Grant No. 51411130127).

References

[1] Veigas M, López M, Iglesias G. Assessing the optimal location for a shoreline wave energy converter. Applied Energy 2014; 132(11):404-11.

[2] Iturrioz A, Guanche R, Armesto JA, et al. Time-domain modeling of a fixed detached oscillating water column towards a floating multi-chamber device. Ocean Engineering 2014; 76: 65-74.

[3] Ning DZ, Teng B, Eatock Taylor R and Zang J. Nonlinear numerical simulation of regular and focused waves in an infinite water depth. Ocean Engineering, 2008, 35:887-899.

[4] Koo WC, Kim MH. Fully nonlinear wave-body interactions with surface-piercing bodies. Ocean Engineering, 2007, 34: 1000-1012.